Journal of Membrane Science 610 (2020) 118268

Contents lists available at ScienceDirect

Journal of Membrane Science

journal homepage: http://www.elsevier.com/locate/memsci

Thin film composite membrane compaction in high-pressure reverse osmosis

Douglas M. Davenport [a], Cody L. Ritt [a], Rhea Verbeke [b], Marcel Dickmann [c], Werner Egger [c], Ivo F.J. Vankelecom [b], Menachem Elimelech [a,*]

[a] Department of Chemical and Environmental Engineering, Yale University, New Haven, CT, 06511, USA
[b] Membrane Technology Group, Centre for Membrane Separations, Adsorption, Catalysis and Spectroscopy for Sustainable Solutions (cMACS), KU Leuven, Celestijnenlaan 200F Box 2454, 3001, Leuven, Belgium
[c] Institut für Angewandte Physik und Messtechnik, Universität der Bundeswehr München, Werner-Heisenberg-Weg 39, München, 85577, Neubiberg, Germany

ARTICLE INFO

Keywords:
Compaction
Water permeability
High-pressure reverse osmosis
Membrane transport
Desalination

ABSTRACT

Membrane deformation under an applied hydraulic pressure, often termed compaction, is observed in almost all pressure-driven membrane processes. Most notably, compaction decreases water permeability in conventional reverse osmosis (RO) and is expected to critically hinder high-pressure reverse osmosis (HPRO) for hypersaline brine desalination. In this work, we demonstrated that compaction decreases the water permeability of commercial RO membranes from 2.0 L m^{-2} h^{-1} bar^{-1} at 70 bar applied hydraulic pressure to 1.3 L m^{-2} h^{-1} bar^{-1} at 150 bar. The morphological effects of compaction were primarily associated with changes in the support layer, where a ~60% decrease in cross-sectional thickness is observed following compaction at 150 bar hydraulic pressure. In contrast, positron annihilation lifetime spectroscopy demonstrates that the selective layer does not compact irreversibly. The mechanism that drives compaction was found to be the difference in hydraulic pressure across the interface of the selective and support layers. We further found that compaction can reduce the support layer surface porosity by up to ~95%. This decreased porosity is identified as the cause for compaction-induced water permeability decline, while the intrinsic permeability of the selective layer is not influenced by compaction. As such, we conclude that compaction of the support layer has an inextricable impact on composite membrane performance. Finally, we propose recommendations for developing compaction-resistant membranes that can maintain high water permeability, and thus good desalination performance, in high-pressure membrane applications, such as HPRO.

1. Introduction

The rising global demand for water and the need to protect environmental water sources will require a renewed focus on wastewater management and beneficial reuse in the coming decades [1]. In particular, more rigorous wastewater treatment is needed from industrial sources to curtail the potential negative effects of unsafe wastewater disposal [2]. High-salinity wastewaters are particularly challenging to treat due to the amalgam of contaminants potentially present at high concentrations, thus requiring unique treatment and management strategies [3]. In some circumstances, increasing economic and regulatory stressors are driving management efforts toward zero liquid discharge (ZLD) and minimal liquid discharge (MLD) brine management practices [4]. For high salinity wastewaters, these practices require brine desalination which currently relies on energy-intensive thermal separation technologies [2].

Recently, high-pressure reverse osmosis (HPRO), has been proposed as an alternative brine desalination and concentration technology [5]. HPRO seeks to leverage the inherent energy efficiency of conventional reverse osmosis (RO) for the desalination of high salinity brines. Conventional RO is limited to a maximum pressure of ~80 bar due to poor membrane performance above this pressure and limitations in module and pressure vessel designs [6]. At 80 bar, saline feed streams can be concentrated to a retentate concentration of ~70,000 mg L^{-1} total dissolved solids (TDS). The retentate stream must then be disposed or desalinated with energy-intensive thermal technologies. In contrast, HPRO operating at hydraulic pressures of 150 bar or 300 bar could potentially reach retentate concentrations of ~150,000 mg L^{-1} TDS or

* Corresponding author.
E-mail address: menachem.elimelech@yale.edu (M. Elimelech).

https://doi.org/10.1016/j.memsci.2020.118268
Received 25 March 2020; Received in revised form 12 May 2020; Accepted 13 May 2020
Available online 30 May 2020

~250,000 mg L^{-1} TDS, respectively [5]. Doing so would minimize the volume of difficult-to-dispose retentate while increasing the quantity of permeate that can be reused. Due to the inherent efficiency of membrane-based processes, HPRO is expected to consume 2- to 3-fold less energy for brine desalination than state-of-the-art thermal desalination technologies [5].

The high pressures and salinities associated with HPRO will incur new design challenges. Namely, novel membrane module and pressure vessel designs may be needed to withstand higher applied pressures. In addition, measures must be taken to control corrosion at high brine concentrations where typical stainless-steel alloys corrode. Inorganic scale formation by sparingly soluble salts must also be mitigated at high water recovery ratios. Despite these challenges, the greatest knowledge gap in the development of HPRO is the impact of high applied pressures on membrane performance and physicochemical properties. Applied pressure is known to cause membrane compaction, or deformation, in conventional RO, resulting in decrements to membrane water permeability. Compaction is likely more severe in HPRO due to the use of increased applied hydraulic pressures, but its effects on membrane structure and water permeability remain unknown.

Compaction is widely observed in all pressure-driven membrane processes, including microfiltration (MF) [7–9], ultrafiltration (UF) [10–12], nanofiltration (NF) [13–15], and RO [16–18]. The decrease in water permeability associated with compaction requires higher applied operating pressures, and thus higher energy consumption, to maintain a constant water flux. Despite the ubiquity of compaction in membrane processes, its fundamental behavior remains poorly understood. Several works have sought to develop a predictive correlation for the relationship between hydraulic pressure, membrane deformation, and water permeability [19–21]. Nevertheless, it is not feasible to develop a universal understanding, that is applicable to all membranes, due to the strong dependence of deformation behavior on varying membrane morphologies and chemical compositions.

The role of compaction becomes more unclear for RO and NF membranes, which typically have a thin film composite (TFC) structure. TFC membranes comprise two distinct layers: the selective layer and the support layer [22,23]. The selective layer is a thin film, typically cross-linked polyamide, with small free-volume elements (diameter ~ 4 Å [24]) which give rise to the membrane's intrinsic water–salt permselectivity. The poor mechanical integrity of this thin polymer layer cannot sustain the applied pressures of NF and RO; therefore, it is formed on a porous support layer (thickness O ~ 100 μm) [25,26]. Polysulfone (PSf) and polyethersulfone (PES) are commonly used support materials due to their simple processability, low cost, and thermal stability [27].

The composite nature of TFC membranes has raised questions about the effects of compaction in both the selective and support layers. In response, several works have developed resistors-in-series or viscoelastic models to describe the cumulative impacts of compaction in each membrane layer [21,28–30]. A highly porous region of the membrane, such as the support layer, is often believed to deform more severely than other membrane components [18–21,30–33]. Accordingly, support layer deformation may contribute substantially to compaction-related decrements in TFC water permeability [18,30]. In addition, deformation at the interface of the support and selective layers has been suggested to reduce the effective membrane surface area, and thus play a dominant role in permeability decline [34]. Furthermore, other studies claim the support layer transport resistance is so low that any change in water permeability must result from compaction of the selective layer—albeit without directly observing selective layer deformation [16,28,29]. As such, there is no clear consensus as to which membrane layers are impacted by compaction and, more importantly, how they influence membrane water permeability.

In this study, we report on the fundamental nature of compaction in TFC membranes and its role to decrease water permeability in pressure-driven membrane processes. A first-of-its-kind bench-scale HPRO apparatus was developed to study compaction at conventional RO pressures (i.e., 70 bar) and in HPRO (i.e., 150 bar). High-resolution electron microscopy enables us to separately characterize the membrane layers impacted by compaction, while also measuring the size of free-volume elements with positron annihilation lifetime spectroscopy. We propose mechanisms to describe compaction in TFC membranes based on experimental evidence presented in this study. Critically, we identify the membrane properties that change in response to compaction and their role in overall water permeability. In doing so, we identify several material properties which must be improved to yield compaction-resistant membranes in order to increase energy efficiency in conventional RO and HPRO.

2. Materials and methods

2.1. Materials

Tri-mesoyl chloride (TMC, 98%), *m*-phenylenediamine (MPD, 99%), and citric acid (ACS reagent grade) were purchased from Sigma Aldrich (St. Louis, MO). Isopropyl alcohol (IPA, ACS reagent grade), hexane (95% n-hexane), and isobutyl alcohol (IBA, ACS reagent grade) were purchased from J.T. Baker (Phillipsburg, NJ). Ethanol (200 proof) was purchased from Decon Laboratories, Inc. (King of Prussia, PA). All reagents were used as received. Deionized water was obtained from a Milli-Q Ultrapure water purification system (Millipore, Billerica, MA).

Commercial SW30-XLE membranes were purchased from Dupont Water Solutions (Wilmington, DE). Sepro PS20 polysulfone (PSf) ultrafiltration membranes were purchased from Sepro Membranes (Oceanside, CA) and used as support layers for TFC membrane fabrication via interfacial polymerization. All membranes were wetted prior to use in an aqueous solution of 25 wt% IPA for 30 min followed by three exchanges of DI water for 30 min each. Wetted membranes were stored in DI water at 4 °C.

2.2. High-pressure reverse osmosis experiments

2.2.1. High-pressure reverse osmosis experimental apparatus

A bench-scale crossflow HPRO apparatus was constructed in order to characterize membranes at hydraulic pressures up to 150 bar (Fig. S1). A pump (Wanner Engineering, Inc., Minneapolis, MN) circulates water from the feed reservoir through a custom-built membrane cell. An in-line polypropylene cartridge filter (1 μm) is located upstream of the pump. The crossflow velocity is controlled by redirecting a portion of the total pump output to bypass the membrane cell. The permeate flowrate (i.e., water flux) is measured with an optical flow meter (Tovatech, Maplewood, NJ). The bypass, permeate, and retentate streams are all returned to the feed reservoir.

The custom-built membrane cell primarily comprises Delrin® acetal resin (Dupont, Wilmington, DE) which has been machined to the desired specifications. Briefly, the membrane is placed between two cell plates which are bolted together. The lower plate contains inlet and outlet ports for the feed and retentate streams, respectively, and a rectangular feed channel that is 7.7 cm long, 2.5 cm wide, and 0.3 cm high. A rectangular gland surrounds the feed channel and contains an O-ring which forms a face seal with the membrane surface when the top cell plate is bolted onto the permeate side of the membrane. A porous stainless-steel frit is embedded in the top cell plate to support the permeate side of the membrane while allowing water to exit the cell from an outlet port behind the frit.

Temperature in the HPRO apparatus is controlled by a recirculating chiller (Cole-Parmer, Vernon Hills, IL) with a cooling coil placed in the feed reservoir. A pressure relief valve (Wanner Engineering, Inc., Minneapolis, MN) is located immediately downstream of the pump to prevent the system from exceeding the pump's pressure rating (170 bar). A real-time pressure control system regulates motor speed to maintain a specified pressure setpoint and halt the pump if the pressure deviates

from a predetermined range. All experiments were performed at a crossflow velocity of 0.33 m s^{-1} and a temperature of 25 °C. Water permeability coefficients of commercially-available membranes are consistent with those presented in previous works [35,36], confirming the reliability of our HPRO setup.

Despite all wetted metal components consisting of type 316 stainless steel, corrosion was occasionally observed. Regular cleaning and repassivation of the stainless steel were performed to restore its corrosion resistance. To do so, the Delrin® membrane test cell was first removed from the system as it is not stable at the pH conditions used during cleaning and repassivation. Dawn® dish soap (Proctor & Gamble, Cincinnati, OH) is then added to the system at an approximate concentration of 0.25 vol% and circulated for 1 h. The system was then thoroughly rinsed with DI water. Citric acid (pH 2) was then circulated for a minimum of 3 h at 25 °C before once again thoroughly rinsing the system with DI water. The HPRO system was then disassembled and air-dried for a minimum of 48 h, allowing atmospheric oxygen to regenerate the chromium oxide passive layer. The system was finally rinsed with DI water and reassembled.

2.2.2. Water permeability measurements

The water permeability of commercial SW30 and TFC membranes fabricated in this study was measured using the HPRO crossflow setup described in Section 2.2.1. Membranes were sealed in the HPRO cell and pressurized with DI water at 30, 70, 110, or 150 bar hydraulic pressure while measuring water flux. The rate of pressure increase was 10 bar s^{-1} and all compaction experiments were performed for 1 h unless otherwise stated.

The water permeability of support layers was not measured by directly exposing a support layer to high hydraulic pressures due to excessive water flux (~1500 L m^{-2} h^{-1}) at 150 bar, which does not accurately represent the flow of water through the support layer of a TFC membrane. As such, support layers were first compacted with an upside-down SW30 membrane placed on the feed side of the membrane at a hydraulic pressure of 30, 70, 110, or 150 bar for 1 h. The SW30 membrane was then removed and the water permeability of each support layer was measured separately at 10 bar hydraulic pressure.

Membranes were supported in all experiments by placing them directly onto the permeate-side porous frit. As such, the impact of permeate spacers was not investigated in this study. Mesh-like permeate spacers have a significant impact on membrane deformation in module-scale applications [37,38]. The goal of this study, however, is to investigate the fundamental nature of compaction in TFC membranes. Thus, the varied and complex role of spacers in membrane compaction is excluded in order to directly examine the morphological impacts of hydraulic pressure on membrane deformation. In doing so, an improved understanding of compaction mechanisms will assist the future development of spacers which minimize deformation in HPRO.

2.3. Microscopy characterization

Membrane morphology was observed using scanning electron microscopy (SEM, Hitachi, SU-70, Hitachi High Technologies America, Inc., Schaumburg, IL) with a 2.0 kV electron acceleration potential and a working distance of 5 mm ± 1 mm. Cross section samples were prepared by immersing a wetted membrane in liquid nitrogen for approximately 60 s then pressing a razor blade against the back side of the membrane to fracture it. All samples were coated with iridium (8.0 nm thickness) using a Cressington Sputter Coater 208 HR (Watford, UK) at a current of 40 mA. Images were adjusted for brightness and contrast using ImageJ software [39].

Samples were prepared for transmission electron microscopy (TEM) by first removing the polyester fabric backing and placing the membrane in three sequential exchanges of ethanol for 15 min each. Membranes were then embedded in LR White resin (Ted Pella, Inc., Redding, CA) by first transferring them to a 1:1 ethanol/resin (v/v) solution for 1 h followed by a 1:2 ethanol/resin (v/v) solution for 2 h. Membranes were then placed in two sequential exchanges of resin for 3 h and 2 h, respectively. Membrane samples were then cut into thin slices and placed in a polytetrafluoroethylene mold (Ted Pella, Inc., Redding, CA) and cured at 65 °C for 15 h. Oxygen was excluded by using Thermanox® coverslips (Ted Pella, Inc., Redding, CA). After curing, 50-nm-thick cross sections were prepared with a diamond knife (2.5 mm Ultra 45°, Diatome) using a Leica Ultramicrotome UC7 (Leica Microsystems, Wetzlar, Germany). Cross sections were mounted onto carbon type-B/formvar coated copper grids (Ted Pella, Inc., Redding, CA). Light-field images were obtained at 11.5 and 20.5 kx magnification using an FEI Tecnai Biotwin (LaB6, 80 kV) TEM. Images were adjusted for brightness and contrast using ImageJ software [39].

Prior to atomic force microscopy (AFM) imaging, membrane samples were allowed to air dry and taped to a clean glass side with double-sided tape. Membrane surface topography was then observed using a Bruker Dimension FastScan AFM with a FastScan-B tip (5 nm tip radius, Bruker, Billerica, MA) in tapping mode at a scan rate of 3 Hz. Images were processed using Nanoscope Analysis v1.9. All images were flattened with a second order flattening protocol and the RMS roughness measured. For each sample, the average roughness of three scans at each of five random locations was used to determine the sample roughness.

2.4. Positron annihilation lifetime spectroscopy

The size of free-volume elements in SW30 selective layers was measured via positron annihilation lifetime spectroscopy (PALS). PALS measurements were performed with the pulsed low energy positron beam system (PLEPS) at the neutron induced positron source Munich (NEPOMUC) located at the FRM-II reactor in Garching, Germany [40–43]. Implantation energies of 0.75, 1.0, and 1.5 keV were used under ultra-high vacuum conditions and lifetime spectra were recorded. The implantation depths at each energy were calculated [44] knowing the polymer density of polyamide to be 1.26 g cm^{-3} [45]. An energy of 1.0 keV corresponds to a mean implantation depth of ~25 nm, indicating it predominately measures voids present in the selective layer. Surface effects and the influence of the support layer were observed at 0.75 and 1.5 keV, respectively. As such, results are only reported for an implantation energy of 1.0 keV. For each spectrum, 4 million counts were collected at a rate of ~10,000 ct s^{-1} and a time resolution of ~250 ps. The measured spectra were deconvoluted from the background signal and the instrument resolution function, which was determined by measuring p-doped SiC, a standard sample with well-known lifetimes. All spectra were evaluated with PALSfit*3* software [46]. The best fitting results are found for models containing four lifetime components (*p*-Ps, free e^{+}, and two *o*-Ps: τ_3 and τ_4) and have good overall fit variances below 1.2.

2.5. Interfacial polymerization of thin film composite membranes

Polyamide TFC membranes were synthesized via interfacial polymerization (IP) on a PSf support layer following our previously reported studies [47,48]. In brief, a wetted PSf support was taped to a clean glass slide with water-proof tape (Fisher Scientific, Inc., Billerica, MA). An aqueous solution of 3.3 wt% MPD was dispensed onto the support layer and allowed to contact it for 120 s. The solution was then discarded and an air knife used to remove any remaining solution. A solution of 0.15 wt % TMC in hexanes was then dispensed onto the support layer and allowed to contact it for 60 s. This solution was then discarded and the membrane was placed vertically for 120 s to air dry. Membranes were finally placed in a water bath at 70 °C for 120 s before storing in DI water at 4 °C.

2.6. Liquid-liquid porosimetry

Pore size distributions (PSDs) of compacted PSf support layers were

measured using a liquid-liquid porosimetry technique [49,50]. Solutions were prepared by mixing equal parts DI water and isobutyl alcohol (IBA) in a separator funnel, shaking vigorously, and allowing the mixture to reach equilibrium after a minimum of 15 h. The aqueous-rich phase was then collected to be used as the wetting liquid and the alcohol-rich phase collected to be the displacement liquid.

Support layers were compacted following the protocol described in Section 2.2.2, with an upside-down SW30 on top of them. Following 1 h of compaction, the support layer was placed in a custom-built dead-end filtration cell which was filled with the previously-prepared wetting liquid. The feed pressure was sequentially increased from 0 to 6.9 bar hydraulic pressure over 5 min to fully wet the membrane with the aqueous-rich wetting liquid. The wetting liquid was then emptied from the feed reservoir and replaced with the alcohol-rich displacement liquid. The pressure was again sequentially increased from 0 to 6.9 bar over 20 min. Permeate flow through the support layer was measured with a custom-built optical drop counter described previously [51]. As the pressure increases, pores of decreasing size will be wetted by the displacement liquid based on the following equation [49]:

$$P = \frac{2\gamma}{r} \tag{1}$$

where P is the applied pressure, γ is the interfacial tension between the two liquids (1.7 mN/m) [49], and r is the wetted pore radius.

The number of pores wetted at each pressure step can be calculated to determine the pore size distribution (PSD). The total flowrate through wetted pores, at any pressure step, is calculated by the following equation [49]:

$$Q_i = \sum_{k=1}^{i} \frac{n_k \pi r_k^4 P_i}{8\eta l} \tag{2}$$

where Q_i is the total flowrate and P_i is the applied pressure at a given pressure step, i, η is the dynamic viscosity of the displacement liquid, and l is the pore length, taken as the membrane thickness measured via SEM. For each pressure step below step i, the number of pores and radii of each pore are given by n_k and r_k, respectively. The number of pores at each pressure step can be calculated with Eq. (2) and, knowing their size with Eq. (1), the PSD can be determined. Knowing the total area of the membrane sample, A_m, the surface porosity (ε) of the membrane can then be calculated by the following equation:

$$\varepsilon = \frac{1}{A_m} \sum_{k=1}^{i} n_k \pi r_k^2 \tag{3}$$

3. Results and discussion

3.1. Compaction of commercial thin film composite membranes in HPRO

3.1.1. Impact of pressure on water permeability

The relationship between applied hydraulic pressure and water permeability is defined by the solution-diffusion transport model for dense membranes [52]. Here, the pure water flux, J_w, through a given membrane is a product of the water permeability coefficient, A, and the difference between the applied hydraulic pressure, ΔP, and the osmotic pressure difference across the membrane. When characterizing the pure water permeability (i.e., with no solutes present), the water permeability coefficient can be calculated directly as $A = \frac{J_w}{\Delta P}$. The water permeability coefficient of a membrane is generally considered to be constant; however, deviations are often observed and most commonly attributed to compaction, fouling, or a combination of the two effects [53].

We measured the water permeability coefficient of SW30, a conventional RO membrane used for seawater desalination, during operation at various hydraulic pressures (Fig. 1A). Our results suggest the greatest effects of compaction occur instantaneously when pressure is applied and very little time-dependent compaction is observed over 12 h (Fig. S2). The water permeability coefficient reaches steady-state in less than 1 h and a strong negative correlation is observed with increasing hydraulic pressure (Fig. 1B). The steady-state water permeability coefficient decreases by 35% from 2.0 L m^{-2} h^{-1} bar^{-1} at 70 bar to 1.3 L m^{-2} h^{-1} bar^{-1} at 150 bar as a result of increased compaction. The decreased water permeability at high applied pressures will lead to reduced water fluxes, consequently increasing energy consumption in conventional RO and HPRO processes.

3.1.2. Impact of pressure on the polysulfone support layer structure

The cross-sectional membrane morphology of compacted SW30 was observed with SEM to understand the impact of hydraulic pressure on membrane deformation (Fig. 1C–G). While SEM is ideal for studying the support layer, its limited resolution prevents it from being a viable technique to study selective layer morphology. As the applied hydraulic pressure is increased, an incremental decrease in the support layer cross-sectional thickness is observed (Fig. 1B). Specifically, the support layer thickness decreases precipitously from 63 μm for pristine SW30 (i.e., no applied pressure) to 26 μm following compaction at 150 bar. For soft porous materials, such as the PSf support layer, a decreased thickness leads to decrements in the void volume, or volumetric porosity [19,54]. This behavior is clearly visible, particularly in the case of finger-like macrovoids which are completely collapsed after compaction at 150 bar.

It is important to note that compaction can be both reversible and irreversible in nature [11,20,55–58]. That is, after the removal of applied pressure, deformed polymer chains may relax slightly such that the effects of compaction are partially reversed. Because this relaxation has been shown to largely occur immediately after pressure release [20,57], SEM is likely only able to observe irreversible compaction. After compaction at high hydraulic pressures, the water permeability of a compacted membrane increases slightly when tested at lower pressures, but remains within 0.2 L m^{-2} h^{-1} bar^{-1} of the water permeability at its highest compaction pressure (Fig. S3). As such, the greatest effects of compaction appear to be irreversible, which has also been demonstrated in literature [20,56,58]. Therefore, the irreversible compaction observed by SEM provides valuable insight into membrane deformation.

An improved understanding of the mechanics behind support layer compaction can be gained when the support layer is considered to be an open-cell polymer foam [30,59]. Cellular solids compact under a compressive load according to four well-defined stages of deformation (Fig. S4) [60,61]: (i) elastic behavior up to a peak stress level where deformation is dominated by elastic (i.e., reversible) bending of cell walls; (ii) post-peak softening, where cell walls begin to deform plastically (i.e., irreversibly); (iii) a plateau region where very little compressive force is needed to increase strain—observed as a decrease in overall thickness—as cells collapse; (iv) a densification region where compressive force must increase substantially to cause further irreversible deformation, resulting from an increase in porous material strength as collapsed cell walls contact each other.

The irreversible deformation observed in SEM (Fig. 1C–G) is evidence that the support layers have compacted beyond their elastic and post-peak softening limits. The significant decrease in membrane thickness indicates support layer deformation likely extends into the plateau region, which is dominated by cell (i.e., pore) collapse. Porous voids remain visible in all SEM cross sections and TFC support layer porosity is measurable following compaction at each hydraulic pressure (discussion provided in Section 3.3.1). This observation suggests the membrane support layer does not reach the densification regime, even after compaction at 150 bar hydraulic pressure.

3.1.3. Impact of pressure on the polyamide selective layer

The size of free-volume elements in TFC membrane selective layers can be measured with PALS. In brief, membranes are exposed to a source of positrons, the antiparticle of electrons. Following thermalization, a

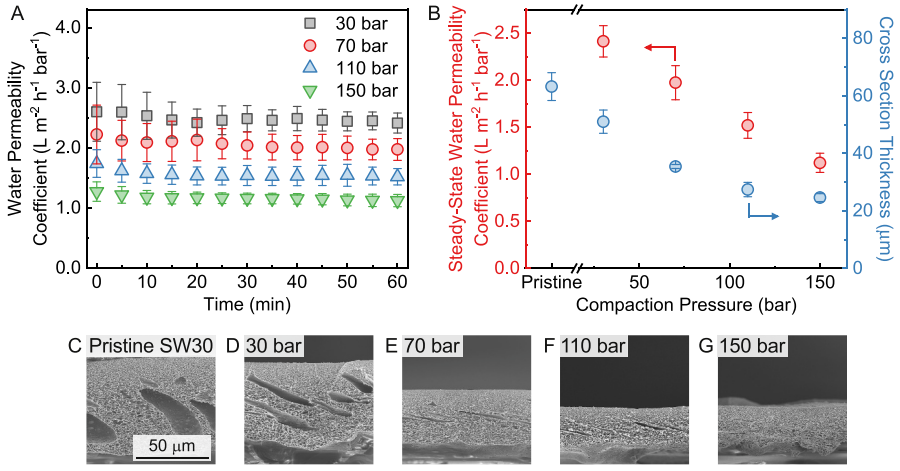

Fig. 1. Characterization of commercially-available SW30 thin film composite membranes following compaction at hydraulic pressures up to 150 bar. Error bars represent the standard deviation of multiple experiments with n ≥ 3. (A) Water permeability coefficient of SW30 at hydraulic pressures up to 150 bar. (B) Steady state water permeability coefficient of SW30 (left axis) and cross-sectional thickness of the polysulfone support layer following compaction (right axis). (C–G) Scanning electron microscope (SEM) cross-sectional images of (C) pristine SW30, (D) SW30 compacted at 30 bar, (E) SW30 compacted at 70 bar, (F) SW30 compacted at 110 bar, and (G) SW30 compacted at 150 bar. All membranes were compacted for 1 h and the scale bar is applicable to all SEM images.

positron may capture an electron and form an unstable hydrogen-like element, positronium (Ps). This particle is trapped inside selective layer free-volume elements until it decays. The lifetime of ortho-Ps (*o*-Ps) can be extracted from the measured PALS spectra and is directly correlated to the size of free-volume elements according to the Tao-Eldrup model [62,63]. Additionally, relative changes in the abundance of free-volume elements can be estimated from the intensity of *o*-Ps lifetimes in some cases.

The average radius of pristine SW30 free-volume elements measured by PALS is 0.246 nm and no significant change is observed following compaction up to 150 bar hydraulic pressure (Fig. 2A). These element radii, measured at a mean implantation depth of ~25 nm, are consistent with other reported values for SW30 [64]. The free-volume element size is independent of compaction pressure, indicating selective layers did not compact irreversibly or undergo a morphological change following the application of high pressure. The intensity of *o*-Ps, an indicator of the relative presence of free-volume elements, is also relatively constant for SW30 membranes at each compaction pressure (Fig. S5). Therefore, despite a decrease in the water permeability of SW30 membranes at high hydraulic pressure (Fig. 1B), PALS proves that compaction does not impact the size and relative quantity of selective layer free-volume elements.

Analysis of the selective layer cross-sectional morphology was conducted with TEM to observe the effects of compaction up to 150 bar hydraulic pressure (Fig. 2B–D and Fig. S6). Here, we observe the traditional ridge-and-valley structure of polyamide films formed via IP. Wrinkling of the resin, marked by dark creases, is found in Fig. 2C and a slight separation between the selective and support layers is observed in Fig. 2D—both common artifacts associated with TEM sample preparation [65]. Critically, there is no evidence of irreversible deformation of the selective layer following compaction at 150 bar when compared to pristine membranes. The total thickness of the selective layer is approximately 200 nm (Fig. 2B) while the nodular base of the polyamide film is roughly 50 nm, typical for RO polyamide films [65–67], regardless of compaction hydraulic pressure.

We further measured the morphology of the selective layer top

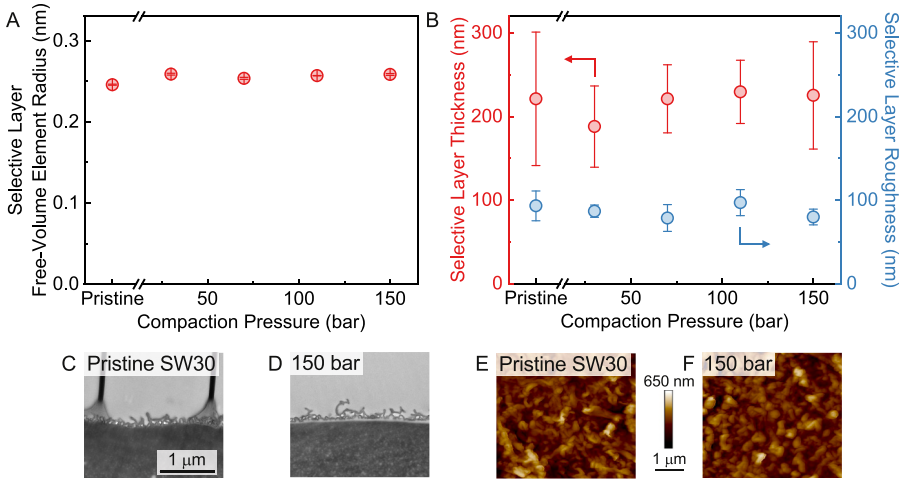

Fig. 2. Characterization of SW30 thin film composite membrane selective layers following compaction at hydraulic pressures up to 150 bar. (A) Selective layer free-volume element radius, corresponding to the τ_3 *o*-Ps lifetime, measured with PALS, as a function of the hydraulic pressure of compaction. The reported values originate from a positron mean implantation depth of ~25 nm. Error bars represent the statistical errors resulting from the measurement data and fitting models. (B) Impact of the hydraulic pressure of compaction on selective layer thickness (from the bottom of the nodular base to the top of ridges present on the film surface at three random locations on three different images) measured from transmission electron microscope (TEM) images (left axis) and R_{RMS} surface roughness measured via atomic force microscopy (AFM) at five random locations (right axis). Error bars represent the standard deviation of multiple measurements. (C–D) TEM cross-sectional images of (C) pristine SW30 and (D) SW30 compacted at 150 bar hydraulic pressure. The ridge-and-valley structures indicate the polyamide selective layer, the dark gray substrate is the electron-dense polysulfone support layer, and the light gray region is the sample embedding resin. The scale bar is applicable to both TEM images. (E–F) AFM surface images of (E) pristine SW30 and (F) SW30 compacted at 150 bar hydraulic pressure. The scale bars are applicable to both AFM images.

surface with AFM. No discernible difference is observed between the pristine and compacted selective layers (Fig. 2E and F and Fig. S7). Specifically, the root mean square roughness (R_{RMS}) of the pristine SW30 membrane is similar to that of compacted membranes (Fig. 2B). This observation is significant because the larger effective membrane surface area provided by a high surface roughness is believed to increase the water permeability of TFC membranes [68]. As such, we can conclude that compaction-induced water permeability decline is not a result of changes in membrane surface roughness. Further, no impact can be seen on the physical characteristics of the polyamide film that were measured in this study (i.e., thickness and roughness), suggesting the selective layer experiences negligible irreversible compaction.

3.2. Elucidating the mechanisms of thin film composite membrane compaction

Our thorough characterization of compacted SW30 membranes illustrates that compaction influences mostly, if not only, the support layer. Despite the evident physical effect of compaction in TFC membranes, its fundamental mechanism remains unknown. Fig. 3A depicts the hydraulic pressure profile assumed by the widely-accepted solution-diffusion model for mass transport in TFC membranes [52]. In this model, hydraulic pressure is constant in the selective layer and equal to the pressure applied to the membrane surface. As a result, the full pressure drop is believed to occur at the interface between the selective and support layers. However, it should be noted that the assumed pressure profile has not been experimentally proven except through validation of the solution-diffusion model [52,69,70].

Following observations that compaction is only observed in support layers, while selective layers appear unchanged, we propose the following mechanism to explain the role of hydraulic pressure to cause compaction in TFC membranes (Fig. 3B and C). The total pressure in compressible porous media is the sum of the fluid hydraulic pressure and any mechanical stress that may be exerted on the solid matrix (i.e., the support layer solid material) [71]. Fig. 3B depicts the role of a difference in hydraulic pressure across the support and selective layer interface, ΔP, to generate a compaction force which is exerted on the solid matrix of the support layer. Immediately when pressure is applied ($t = 0$), a pressure difference exists such that the hydraulic pressure acting on the selective layer, P_A, is much higher than the hydraulic pressure inside the support layer, P_i. This difference in hydraulic pressures generates a force, F_A, that is exerted onto the region of lower hydraulic pressure (i.e., the support layer). This force will act on the support layer solid matrix, increasing mechanical stress, until it is balanced by an equivalent reaction force in the opposite direction, F_R, which arises due to deformation of the support layer solid matrix (Fig. 3C). This mechanical stress generates a reaction force in the support layer as a result of, amongst others, a recoil force due to polymer chain elongation, increased chain entanglement, or steric hinderance as polymer chains contact one another [72–75].

Several experiments were performed to validate the compaction mechanisms proposed in this study. First, two SW30 membranes—stacked with their selective layers facing each other—were compacted at 150 bar hydraulic pressure (Fig. 4A). SEM images show the bottom membrane compacted substantially more than the upside-down membrane. A high cross-sectional thickness and the presence of macrovoids in the top membrane indicate it did not compact when hydraulic pressure was applied to the support layer side of the membrane. This behavior can be quantified by placing a PSf support layer on top of a TFC SW30 membrane (Fig. 4B). These stacked membranes were compacted at hydraulic pressures up to 150 bar before they were separated. Their water permeabilities were then measured individually at 10 bar hydraulic pressure. The water permeability of the PSf support layer remained unchanged after compaction; whereas, the water permeability coefficient of SW30 decreased as a function of the hydraulic pressure of compaction (Fig. 4B).

These results support the proposed mechanism that a difference in hydraulic pressure is needed to generate a compaction force that exerts

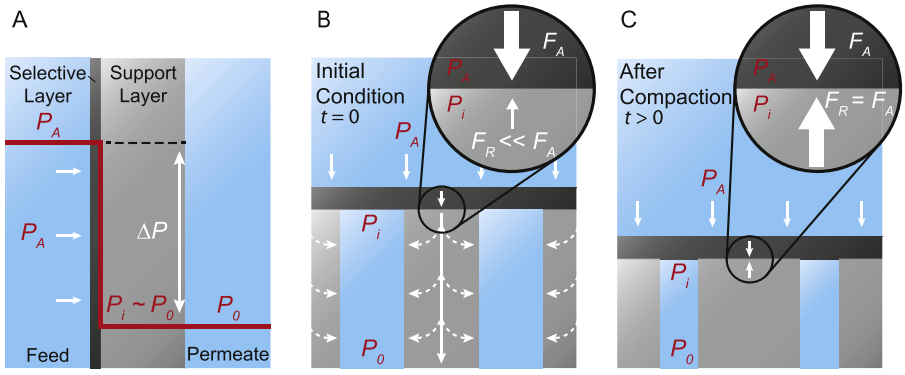

Fig. 3. Schematic depicting compaction mechanisms in TFC membranes. Red labels represent hydraulic pressures and white arrows signify forces. (A) The hydraulic pressure gradient across the selective and support layers of a thin film composite membrane based on the solution-diffusion model. Here, P_A is the applied hydraulic pressure, P_i is the hydraulic pressure inside the support layer, P_0 is the hydraulic pressure of the permeate (i.e., atmospheric pressure), and ΔP is the hydraulic pressure differential between P_A and P_i. The pressure profile depicted here follows the solution-diffusion model which assumes the hydraulic pressure in the selective layer is equal to the applied hydraulic pressure [52]. (B) The effect of a hydraulic pressure difference to generate a compaction force acting on the support layer. Immediately when pressure is applied ($t = 0$), the hydraulic pressure difference between the feed-side applied pressure, P_A, and the hydraulic pressure inside the membrane, P_i, causes a force, F_A, to be applied across the selective layer–support layer interface. This force is much greater than the reaction force, F_R, of the support layer, and thus F_A is applied to the support layer solid matrix, which causes deformation. (C) At $t > 0$, the compacted support layer deforms such that it generates a reaction force, F_R, exerted on the selective layer. When compaction reaches steady state, the mechanical stress of the support layer generates a reaction force that balances the applied force, F_A, and prevents further membrane deformation. (For interpretation of the references to colour in this figure legend, the reader is referred to the Web version of this article.)

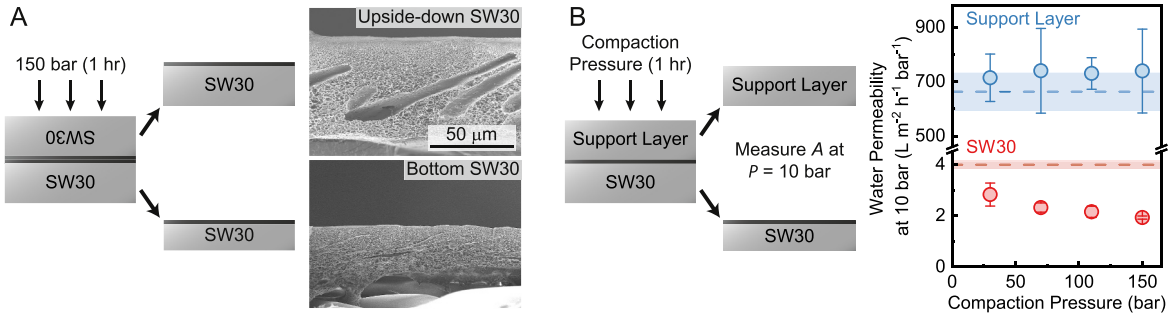

Fig. 4. Experimental evaluation of the role of a difference in hydraulic pressure to cause compaction. (A) Schematic detailing the experimental design of stacking two TFC membranes (SW30) with their selective layers facing each other (left). Membranes were compacted at 150 bar for 1 h and separated to be imaged by SEM (right). The scale bar is representative of both SEM images. (B) Schematic detailing the experimental design of stacking a commercial PSf support layer on top of a TFC membrane (SW30) (left). Membranes were compacted for 1 h at different hydraulic pressures and then separated before the water permeability of each membrane was measured at 10 bar hydraulic pressure. The water permeability of the support layers and SW30 membranes, measured at 10 bar, following compaction at higher hydraulic pressures is shown (right). Dashed lines represent the water permeability coefficient at 10 bar hydraulic pressure of pristine support layers and SW30 membranes which were not compacted in a stacked membrane configuration. Error bars and shaded regions—corresponding to compacted and pristine membranes, respectively—represent the standard deviation of repeated experiments with n ≥ 3.

mechanical stress on the support layer solid matrix. In both stacked membrane configurations, a very small hydraulic pressure gradient exists across the support layer of the top membrane, owing to its high porosity relative to the dense selective layer underneath. As a result, the entirety of the hydraulic pressure drop is across the selective layer(s) of the SW30 membrane(s). According to our mechanism, this difference in hydraulic pressure generates a compressive force acting on the support layer solid matrix below, causing compaction in the bottom membrane. In contrast, the support layer of the top membrane, although filled with a high hydraulic pressure fluid, does not compact because there is a very small hydraulic pressure gradient across it.

Although the hydraulic pressure difference across the selective layer drives compaction, its effects are only observed in the support layer. This is partly because the dense, highly-crosslinked selective layer is more mechanically robust than the porous support layer [30]. TFC support layer compaction may also be more severe, as compared to porous MF or UF membranes, because the water inside the support layer has a very low hydraulic pressure. In contrast, the large pressure gradient across MF and UF membranes causes their internal hydraulic pressure to be greater than that of TFC support layers, which may act to minimize the effects of compaction (Fig. S8). Further, the pressure profile assumed by the solution-diffusion model, if accurate, would preclude selective layer compaction because there is no hydraulic pressure difference across it. Rather, the hydraulic pressure difference exists at the interface of the selective layer and support layer, which then generates a compaction force that could only deform the support layer.

3.3. Relating thin film composite membrane water permeability to membrane structure

3.3.1. Support layer structural and transport properties following compaction

The mechanism proposed in Section 3.2 explains why compaction is observed in the support layer, but it does not explain how it causes a decrease in membrane water permeability. To understand this phenomenon, the compaction behavior of support layers was studied independently and related to overall TFC membrane compaction. Doing so required the synthesis of TFC membranes on commercial PSf support layers. This allowed for the direct comparison of composite membrane properties to those of its underlying support. TFC membranes compacted up to 150 bar hydraulic pressure (Fig. 5) displayed a similar trend in steady-state water permeability to that of SW30 (Fig. S9), indicating these membranes closely match the performance of commercially-available membranes. Support layers were also compacted up to 150 bar hydraulic pressure with an upside-down SW30 membrane placed above them to cause compaction in the support (Fig. S10). After compaction at high pressure, the SW30 was removed and the compacted support layer water permeability was measured at 10 bar hydraulic pressure. The water permeabilities of compacted support layers do not follow the same trend as compacted TFC membranes; instead, they decrease dramatically as a function of pressure (Fig. 5).

Given that water transport in support layers is governed by convective flow through open pores [76], pore size distributions (PSDs) of compacted support layers were measured to understand their water permeability behavior. The distribution of pore sizes follows a binomial distribution with a slight positive skew (Fig. 6). This characteristic shape is similar regardless of the hydraulic pressure of compaction and does not shift to smaller or larger pore sizes as a result of compaction. As such, compaction does not appear to impact the size of pores on the support layer surface. Rather, compaction significantly reduces the quantity of pores, and thus support layer surface porosity (ε), as a function of hydraulic pressure. Drawing from an understanding of open-cell foam deformation (as described in Section 3.1.2), compaction appears to

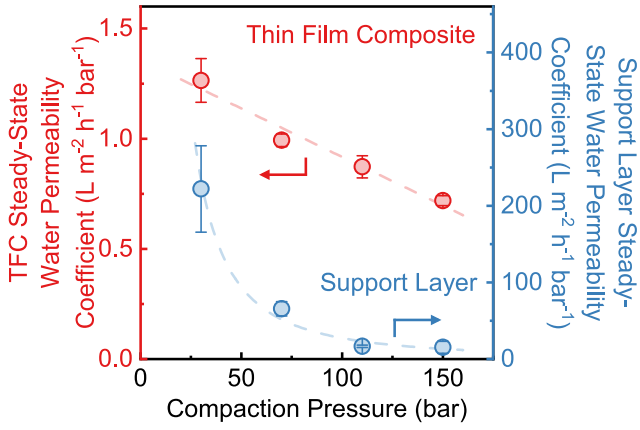

Fig. 5. Steady-state water permeability coefficients of TFC membranes (left axis) and support layers (right axis) following compaction at hydraulic pressures up to 150 bar. TFC membrane water permeability was measured at the specified hydraulic pressure of compaction after 1 h. Support layers were compacted with an upside-down SW30 membrane stacked on their top surface. After 1 h of compaction at the specified hydraulic pressure, the SW30 membrane was removed and the support layer water permeability was measured at 10 bar hydraulic pressure. Lines are drawn to guide the reader's eye. Error bars represent the standard deviation of repeated experiments with n ≥ 3.

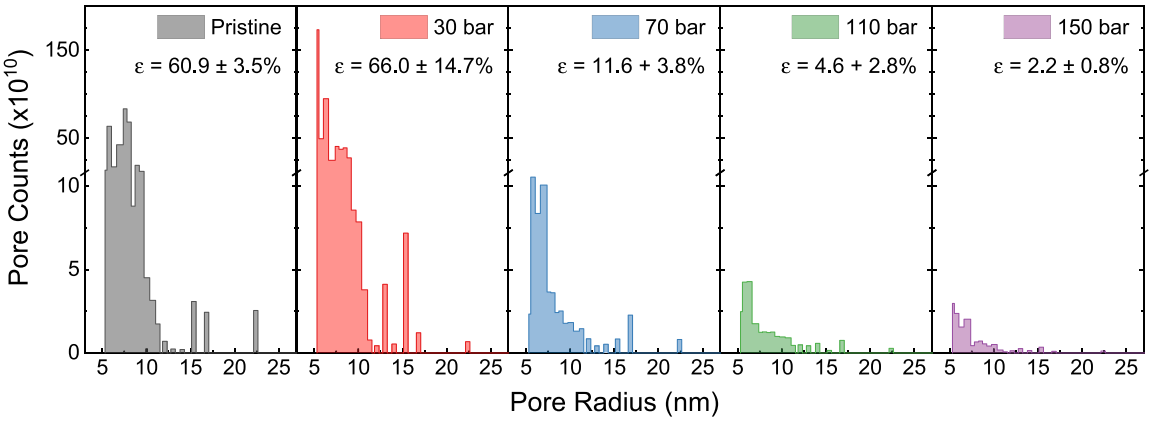

Fig. 6. Pore size distributions (PSDs) of pristine and compacted polysulfone support layers. Membranes were compacted with an upside-down SW30 membrane facing their top surface at hydraulic pressures up to 150 bar. The SW30 membrane was then removed and support layers were characterized alone. Pore counts and surface porosity, ε, were measured using a liquid-liquid porosimetry method described in Section 2.6. Due to experimental limitations, pores with a radius smaller than 5.3 nm could not be measured. A change in scale on the vertical axis scale is shown so PSDs would be visible when low pore counts are present. The PSDs presented here represent the average of repeated experiments with n ≥ 3.

deform the pore walls of the support layer such that some pores become completely blocked while others do not fully collapse.

3.3.2. *Influence of support layer compaction on composite membrane transport*

Compaction significantly impacts support layer morphology and transport properties; however, a decrease in support layer permeability does not translate to a proportional change in TFC membrane permeability. This behavior arises from the composite nature of TFC membranes, as water transport through each membrane layer is governed by distinct behavior. Namely, selective layer transport is controlled by the rate of partitioning into and diffusion across a dense film [52]. In contrast, transport in the support layer occurs as a result of convective flow along a very small hydraulic pressure gradient, similar to MF and UF membranes [22,77,78].

To bring clarity to the composite nature of TFC membrane transport, a model has been proposed to explain the impact of support layer porosity on selective layer transport [18,79,80]. This model assumes that all water permeating the support layer must pass through open pores and not through the support layer polymer phase. Therefore, diffusing species in the selective layer of a TFC membrane must follow preferential flow paths to an open pore in the support layer (Fig. S11). In effect, the pore size and surface porosity of the support layer can substantially impact the diffusive path length, and thus the rate of diffusion, for species permeating the selective layer [80,81].

Owing to the presence of preferential flow paths through the selective layer, an effective selective layer thickness, Δx_{eff}, can be estimated which is greater than the actual selective layer thickness, Δx. These values can then be used to calculate the intrinsic water permeability coefficient of the selective layer, A_{int}, from the observed water permeability coefficient measured experimentally, A_{obs} (calculations provided in the supplementary data). Table 1 reports the results of this analysis for TFC membranes and their support layers following compaction up to 150 bar hydraulic pressure. The support layer pore radius was chosen as the most abundant pore size measured in PSDs (Fig. 6). The selective layer thickness—taken as the polyamide nodular base thickness—is 50 nm, representing measurements from TEM images which are in agreement with previously published works [65–67].

Table 1 reports that decrements in support layer surface porosity are closely linked to increases in the effective selective layer thickness. This behavior arises because a lower porosity requires transporting species to follow an increased diffusive path length through the selective layer before reaching an open pore in the support layer. When Δx_{eff} is related to the decrease in A_{obs} as a function of pressure, the intrinsic water permeability of the selective layer is calculated to be approximately constant. This observation indicates that diffusive transport across the selective layer is not affected by the hydraulic pressure of compaction, thus corroborating that compaction does not appear to impact the selective layer. In contrast, these results indicate that deformation of the support layer, although it has a lower transport resistance than the selective layer, is the primary cause for compaction-related TFC water permeability declines.

The profound implications of these semi-quantitative results offer support for our previous experimental observations. Specifically,

Table 1
Support layer properties as a function of compaction and their impact on TFC membrane transport properties. The range of results represents the standard deviation of repeated experiments with n ≥ 3.

Compaction Pressure (bar)	Support Layer Surface Porosity[a], ε	Support Layer Pore Radius[b], r (nm)	Selective Layer Thickness[c], Δx (nm)	Effective Selective Layer Thickness[d], Δx_{eff} (nm)	Observed TFC Water Permeability[e], A_{obs} (L m^{-2} h^{-1} bar^{-1})	Intrinsic TFC Water Permeability[d], A_{int} (L m^{-2} h^{-1} bar^{-1})
Pristine	60.9 ± 3.5%	6.5 ± 0.9	50.0	51.5 ± 0.1	–	–
30	66.0 ± 14.7%	6.2 ± 1.4	50.0	51.4 ± 1.3	1.26 ± 0.10	1.30 ± 0.03
70	11.6 ± 3.8%	6.1 ± 0.5	50.0	64.7 ± 2.4	0.99 ± 0.03	1.28 ± 0.05
110	4.6 ± 2.8%	5.6 ± 0.4	50.0	78.9 ± 9.9	0.87 ± 0.05	1.37 ± 0.17
150	2.2 ± 0.8%	5.8 ± 0.7	50.0	93.5 ± 8.6	0.72 ± 0.02	1.35 ± 0.12

[a] Calculated from liquid-liquid porosimetry results (Fig. 6).
[b] The most abundant pore size in the PSD (Fig. 6).
[c] Cross-sectional thickness of the nodular base observed in TEM images (Fig. 2C and D and Fig. S6) and reported in literature [65–67].
[d] Calculations provided in supplementary data.
[e] Measurements reported in Fig. 5.

compaction primarily impacts the support layer while the selective layer appears to remain unchanged. The mechanism presented in Section 3.2 states that compaction does not impact the selective layer due to the constant hydraulic pressure maintained across it. Our analysis of compacted support layers and TFC membranes experimentally supports this mechanism, suggesting the intrinsic water permeability of selective layers has little-to-no dependence on the applied hydraulic pressure, indicating compaction has not occurred in the selective layer. As such, it is possible that a decrease in support layer surface porosity may be entirely responsible for compaction-induced decrements to membrane water permeability.

3.4. Implications for the design of compaction-resistant membranes

The results of this study indicate compaction occurs entirely in the support layer of a TFC membrane and that the selective layer does not compact irreversibly. Therefore, compaction-resistant TFC membranes will require support layers with improved mechanical properties to avoid significant deformation under an applied hydraulic pressure. Support layers may be able to achieve these targets through optimization of support morphology or the use of high-strength materials.

To yield compaction-resistant membranes, support layer strength must be improved such that membrane deformation is minimized under increased hydraulic pressures. Although it is not fully representative of all mechanical properties, elastic modulus is an important property as it is related to material stiffness and is often easily measured and reported [82]. By increasing the support layer elastic modulus, a greater force would be required to deform the support layer over a certain distance. In addition, materials with higher stiffness often exhibit a higher yield strength, meaning the material can be stressed with greater force without deforming plasticly. Increasing these properties would allow membranes to sustain higher applied pressures without the negative effects of deformation on support layer porous structures. Due to the application of pressure perpendicular to the membrane surface, improving compressive modulus is likely important to prevent water permeability decline. In industrial-scale applications, however, membranes are often supported by mesh-like spacers. These spacers cause nonuniform membrane compression giving rise to tensile stress in addition to compressive stress, resulting in complex compaction behavior [61]. As such, optimized spacer designs with reduced mesh size may be needed as well as membranes with an increased tensile elastic modulus [83].

The morphology of porous materials significantly impacts their mechanical properties [60] and it is possible an optimized structure will improve support layer compaction resistance. Support layers should be fabricated without macrovoids, believed to be the weakest points in a porous support [32,84], to prevent membrane deformation and decrements in volumetric porosity. Studies on the mechanical strength of cellular solids and foams indicate a microporous structure with uniform, small porous voids should be stronger than one with structural irregularities and large voids [75,85,86]. In polymer foam materials, the elastic modulus, E^*, is related to the density of the foam, ρ^*, according to

$$\frac{E^*}{E_s} \approx \left(\frac{\rho^*}{\rho_s}\right)^2 \quad (4)$$

where E_s and ρ_s are the elastic modulus and density of the solid polymer, respectively [61]. This relationship indicates that maximizing the support layer volumetric mass density (i.e., minimizing the volumetric porosity) would improve the elastic modulus of the support layer. Doing so, however, will likely hinder water permeability through the membrane. As such, it is possible that a trade-off may exist wherein improvements in support layer mechanical properties come at the expense of membrane permeability.

The challenges of optimizing support layer structure to improve compaction resistance may be avoided by utilizing unconventional membrane materials. Eq. (4) indicates the elastic modulus of a porous material is improved when it is synthesized from a stronger solid material [61]. Therefore, it may be necessary to employ materials with a higher elastic modulus than PSf and PES for the synthesis of compaction-resistant support layers. Such materials may include semi-crystalline polymers or copolymers tailored to yield strong and easily-processable materials for the development of polymeric supports. Alternatively, ceramic materials, which are largely incompressible, have been used as supports for TFC membranes and may be ideal for HPRO applications [87]. However, it should be noted that brittle fracture may occur in ceramic supports at high pressures, which would lead to failure of the membrane module. The use of any novel support layer material will also have implications on selective layer formation and performance. Support layer pore size, porosity, and hydrophilicity must be carefully controlled in order to create a support that yields viable selective layers during IP [27,88].

Our results indicate support layers must maintain a high surface porosity when hydraulic pressure is applied to prevent compaction-induced water permeability decline. For example, our support layers had surface porosities of 11.6% and 2.2% following compaction at 70 bar and 150 bar, respectively. If a support layer could maintain a surface porosity of ~12% after compaction at 150 bar, the membrane may avoid the detrimental performance effects caused by compaction. As such, novel material designs with a surface pore structure that is unaffected by applied pressure may maintain high water permeabilities despite compaction of the underlying support.

In contrast to the critical need for novel support layer morphologies and materials, the optimal selective layer may continue to be the traditional polyamide film formed by IP. The apparent absence of compaction within the selective layer of a TFC membrane suggests any material with the desired separation capacity may be used. Therefore, polyamide films formed by IP are likely the best choice in desalination applications as their performance has been optimized to achieve high water permeability and salt rejection.

4. Conclusion

Compaction at high applied pressures significantly reduces water permeability in conventional RO and HPRO. For the first time, we have experimentally measured the influence of compaction on commercial desalination membranes at hydraulic pressures relevant to HPRO (150 bar). The greatest effects of compaction are observed in the support layer of TFC membranes while selective layers do not compact irreversibly, as confirmed by PALS analysis. To explain this behavior, we propose a mechanism to describe the fundamental role of a difference in hydraulic pressure to cause compaction in TFC membranes. The classic solution-diffusion model states that this hydraulic pressure difference is located at the interface between the selective and support layers. This hydraulic pressure imbalance generates a compaction force that is exerted on the support layer until it deforms to the extent that an equivalent reaction force is generated. Such deformation reduces the cross-sectional thickness and surface porosity of the support layer, while it does not affect these properties in the selective layer. The surface porosity of the support layer was determined to be an important physical characteristic related to compaction. Specifically, a decrease in support layer surface porosity increases the diffusive path length of water permeating the selective layer, while the intrinsic water permeability of the selective layer is independent of compaction. By relating the physical characteristics of the support layer to the total membrane water permeability, we identified membrane properties which are expected to minimize compaction. We further highlight that the design of compaction-resistant membranes should focus on improving support layer deformation resistance. In doing so, a compaction-resistant membrane will be able to maintain operationally feasible water permeabilities at high hydraulic pressures, thus improving the energy efficiency of conventional RO and HPRO processes.

Declaration of competing interest

The authors declare that they have no competing financial interests that could have appeared to influence the work reported in this paper.

CRediT authorship contribution statement

Douglas M. Davenport: Conceptualization, Data curation, Formal analysis, Writing - original draft, Writing - review & editing. **Cody L. Ritt:** Data curation, Formal analysis, Writing - review & editing. **Rhea Verbeke:** Formal analysis, Writing - review & editing. **Marcel Dickmann:** Data curation. **Werner Egger:** Data curation. **Ivo F.J. Vankelecom:** Supervision. **Menachem Elimelech:** Supervision.

Acknowledgements

This work was supported by the National Science Foundation under Grant CBET-1701658. R.V. thanks Research Foundation Flanders (FWO) for a SB-PhD fellowship (1S00917N) and for a travel grant (V406619N). Facilities used for SEM, TEM, and AFM were provided by the Yale Institute of Nanoscale and Quantum Engineering (YINQE). PALS experiments were performed at the NEPOMUC PLEPS instrument operated by FRM-II at the Heinz MaierLeibnitz Zentrum (MLZ) in Garching, Germany. We would also like to thank Evyatar Shaulsky for his assistance constructing the high-pressure reverse osmosis apparatus used in this study.

Appendix A. Supplementary data

Supplementary data to this article can be found online at https://doi.org/10.1016/j.memsci.2020.118268.

References

[1] A Post-2015 Global Goal for Water: Synthesis of Key Findings and Recommendations from UN-water, United Nations Water, New York, NY, 2014.
[2] T. Tong, M. Elimelech, The global rise of zero liquid discharge for wastewater management: drivers, technologies, and future directions, Environ. Sci. Technol. 50 (2016) 6846–6855.
[3] O. Lefebvre, R. Moletta, Treatment of organic pollution in industrial saline wastewater: a literature review, Water Res. 40 (2006) 3671–3682.
[4] Z. Wang, A. Deshmukh, Y. Du, M. Elimelech, Minimal and zero liquid discharge with reverse osmosis using low-salt-rejection membranes, Water Res. 170 (2020) 115317.
[5] D.M. Davenport, A. Deshmukh, J.R. Werber, M. Elimelech, High-pressure reverse osmosis for energy-efficient hypersaline brine desalination: current status, design considerations, and research needs, Environ. Sci. Technol. Lett. 5 (2018) 467–475.
[6] C. Fritzmann, J. Löwenberg, T. Wintgens, T. Melin, State-of-the-art of reverse osmosis desalination, Desalination 216 (2007) 1–76.
[7] C. Mu, Y. Su, M. Sun, W. Chen, Z. Jiang, Remarkable improvement of the performance of poly(vinylidene fluoride) microfiltration membranes by the additive of cellulose acetate, J. Membr. Sci. 350 (2010) 293–300.
[8] W. Richard Bowen, Q. Gan, Microfiltration of protein solutions at thin film composite membranes, J. Membr. Sci. 80 (1993) 165–173.
[9] S. Chellam, G. Jacangelo Joseph, Existence of critical recovery and impacts of operational mode on potable water microfiltration, J. Environ. Eng. 124 (1998) 1211–1219.
[10] H. Susanto, M. Ulbricht, Characteristics, performance and stability of polyethersulfone ultrafiltration membranes prepared by phase separation method using different macromolecular additives, J. Membr. Sci. 327 (2009) 125–135.
[11] D.M. Bohonak, A.L. Zydney, Compaction and permeability effects with virus filtration membranes, J. Membr. Sci. 254 (2005) 71–79.
[12] V.R. Tarnawski, P. Jelen, Estimation of compaction and fouling effects during membrane processing of cottage cheese whey, J. Food Eng. 5 (1986) 75–90.
[13] R. Heffernan, A.J.C. Semião, P. Desmond, H. Cao, A. Safari, O. Habimana, E. Casey, Disinfection of a polyamide nanofiltration membrane using ethanol, J. Membr. Sci. 448 (2013) 170–179.
[14] L.M. Ortega, R. Lebrun, I.M. Noël, R. Hausler, Application of nanofiltration in the recovery of chromium (III) from tannery effluents, Separ. Purif. Technol. 44 (2005) 45–52.
[15] D. Nanda, K.-L. Tung, Y.-L. Li, N.-J. Lin, C.-J. Chuang, Effect of pH on membrane morphology, fouling potential, and filtration performance of nanofiltration membrane for water softening, J. Membr. Sci. 349 (2010) 411–420.
[16] H. Mehdizadeh, J.M. Dickson, P.K. Eriksson, Temperature effects on the performance of thin-film composite, aromatic polyamide membranes, Ind. Eng. Chem. Res. 28 (1989) 814–824.
[17] S. Kimura, Analysis of reverse osmosis membrane behaviors in a long-term verification test, Desalination 100 (1995) 77–84.
[18] M.T.M. Pendergast, J.M. Nygaard, A.K. Ghosh, E.M.V. Hoek, Using nanocomposite materials technology to understand and control reverse osmosis membrane compaction, Desalination 261 (2010) 255–263.
[19] Y. Kurokawa, M. Kurashige, N. Yui, A viscoelastic model for initial flux decline through reverse osmosis membrane, Desalination 52 (1984) 9–14.
[20] R.A. Peterson, A.R. Greenberg, L.J. Bond, W.B. Krantz, Use of ultrasonic TDR for real-time noninvasive measurement of compressive strain during membrane compaction, Desalination 116 (1998) 115–122.
[21] H. Ohya, An expression method of compaction effects on reverse osmosis membranes at high pressure operation, Desalination 26 (1978) 163–174.
[22] R.W. Baker, Membrane Technology and Applications, McGraw-Hill, New York, NY, 2000.
[23] J.E. Cadotte, R.J. Petersen, R.E. Larson, E.E. Erickson, A new thin-film composite seawater reverse osmosis membrane, Desalination 32 (1980) 25–31.
[24] R. Verbeke, V. Gómez, T. Koschine, S. Eyley, A. Szymczyk, M. Dickmann, T. Stimpel-Lindner, W. Egger, W. Thielemans, I.F.J. Vankelecom, Real-scale chlorination at pH4 of BW30 TFC membranes and their physicochemical characterization, J. Membr. Sci. 551 (2018) 123–135.
[25] J.R. Werber, C.O. Osuji, M. Elimelech, Materials for next-generation desalination and water purification membranes, Nat. Rev. Mater. 1 (2016) 16018.
[26] S.S. Manickam, J. Gelb, J.R. McCutcheon, Pore structure characterization of asymmetric membranes: non-destructive characterization of porosity and tortuosity, J. Membr. Sci. 454 (2014) 549–554.
[27] A.K. Ghosh, E.M.V. Hoek, Impacts of support membrane structure and chemistry on polyamide–polysulfone interfacial composite membranes, J. Membr. Sci. 336 (2009) 140–148.
[28] Y.A. Hussain, M.H. Al-Saleh, S.S. Ar-Ratrout, The effect of active layer non-uniformity on the flux and compaction of TFC membranes, Desalination 328 (2013) 17–23.
[29] Y.A. Hussain, M.H. Al-Saleh, A viscoelastic-based model for TFC membranes flux reduction during compaction, Desalination 344 (2014) 362–370.
[30] M. Aghajani, M. Wang, L.M. Cox, J.P. Killgore, A.R. Greenberg, Y. Ding, Influence of support-layer deformation on the intrinsic resistance of thin film composite membranes, J. Membr. Sci. 567 (2018) 49–57.
[31] G. Belfort, G. Alexandrowicz, B. Marx, Artificial particulate fouling of hyperfiltration membranes, Desalination 19 (1976) 127–138.
[32] K.M. Persson, V. Gekas, G. Trägårdh, Study of membrane compaction and its influence on ultrafiltration water permeability, J. Membr. Sci. 100 (1995) 155–162.
[33] J.A. Idarraga-Mora, A.S. Childress, P.S. Friedel, D.A. Ladner, M.A. Rao, M. S. Husson, Role of nanocomposite support stiffness on TFC membrane water permeance, Membranes 8 (2018).
[34] X. Chen, C. Boo, N.Y. Yip, Transport and structural properties of osmotic membranes in high-salinity desalination using cascading osmotically mediated reverse osmosis, Desalination 479 (2020) 114335.
[35] J.R. Werber, A. Deshmukh, M. Elimelech, The critical need for increased selectivity, not increased water permeability, for desalination membranes, Environ. Sci. Technol. Lett. 3 (2016) 112–120.
[36] R. Rautenbach, T. Linn, L. Eilers, Treatment of severely contaminated waste water by a combination of RO, high-pressure RO and NF — potential and limits of the process, J. Membr. Sci. 174 (2000) 231–241.
[37] J. Johnson, M. Busch, Engineering aspects of reverse osmosis module design, Desalinat. Water Treat. 15 (2010) 236–248.
[38] Q. She, D. Hou, J. Liu, K.H. Tan, C.Y. Tang, Effect of feed spacer induced membrane deformation on the performance of pressure retarded osmosis (PRO): implications for PRO process operation, J. Membr. Sci. 445 (2013) 170–182.
[39] W.S. Rasband, ImageJ, U.S. National Institutes of Health, Bethesda, Maryland, USA, 1997-2016.
[40] C. Hugenschmidt, G. Dollinger, W. Egger, G. Kögel, B. Löwe, J. Mayer, P. Pikart, C. Piochacz, R. Repper, K. Schreckenbach, P. Sperr, M. Stadlbauer, Surface and bulk investigations at the high intensity positron beam facility NEPOMUC, Appl. Surf. Sci. 255 (2008) 29–32.
[41] C. Hugenschmidt, C. Piochacz, M. Reiner, K. Schreckenbach, The NEPOMUCupgradeand advanced positron beam experiments, New J. Phys. 14 (2012), 055027.
[42] W. Egger, P. Sperr, G. Kögel, G. Dollinger, Pulsed low energy positron system (PLEPS) at the Munich research reactor FRM II, Phys. Status Solidi C 4 (2007) 3969–3972.
[43] P. Sperr, W. Egger, G. Kögel, G. Dollinger, C. Hugenschmidt, R. Repper, C. Piochacz, Status of the pulsed low energy positron beam system (PLEPS) at the Munich Research Reactor FRM-II, Appl. Surf. Sci. 255 (2008) 35–38.
[44] J. Algers, P. Sperr, W. Egger, G. Kögel, F.H.J. Maurer, Median implantation depth and implantation profile of 3–18 keV positrons in amorphous polymers, Phys. Rev. B 67 (2003) 125404.
[45] L. Lin, C. Feng, R. Lopez, O. Coronell, Identifying facile and accurate methods to measure the thickness of the active layers of thin-film composite membranes – a comparison of seven characterization techniques, J. Membr. Sci. 498 (2016) 167–179.
[46] P. Kirkegaard, J.V. Olsen, M.M. Eldrup, PALSfit3: a software package for analysing positron lifetime spectra, in: Technical University of Denmark, Kgs. Lyngby, 2017.
[47] J.R. Werber, S.K. Bull, M. Elimelech, Acyl-chloride quenching following interfacial polymerization to modulate the water permeability, selectivity, and surface charge of desalination membranes, J. Membr. Sci. 535 (2017) 357–364.

[48] C. Boo, Y. Wang, I. Zucker, Y. Choo, C.O. Osuji, M. Elimelech, High performance nanofiltration membrane for effective removal of perfluoroalkyl substances at high water recovery, Environ. Sci. Technol. 52 (2018) 7279–7288.
[49] J.I. Calvo, A. Bottino, G. Capannelli, A. Hernández, Comparison of liquid–liquid displacement porosimetry and scanning electron microscopy image analysis to characterise ultrafiltration track-etched membranes, J. Membr. Sci. 239 (2004) 189–197.
[50] R.I. Peinador, J.I. Calvo, P. Prádanos, L. Palacio, A. Hernández, Characterisation of polymeric UF membranes by liquid–liquid displacement porosimetry, J. Membr. Sci. 348 (2010) 238–244.
[51] K.R. Zodrow, V.H. Coulter, E. Shaulsky, M. Elimelech, Low flow data logger in membrane distillation: an interdisciplinary laboratory in process control, in: Fourth Interdisciplinary Engineering Design Education Conference, 2014, pp. 70–73.
[52] J.G. Wijmans, R.W. Baker, The solution-diffusion model: a review, J. Membr. Sci. 107 (1995) 1–21.
[53] L.J. Bond, A.R. Greenberg, A.P. Mairal, G. Loest, J.H. Brewster, W.B. Krantz, Real-time nondestructive characterization of membrane compaction and fouling, in: D. O. Thompson, D.E. Chimenti (Eds.), Review of Progress in Quantitative Nondestructive Evaluation, vol. 14, Springer US, Boston, MA, 1995, pp. 1167–1173.
[54] M. Kurashige, Transient response of a fluid-saturated poroelastic layer subjected to a sudden fluid pressure rise, J. Appl. Mech. 49 (1982) 492–496.
[55] L. Brinkert, N. Abidine, P. Aptel, On the relation between compaction and mechanical properties for ultrafiltration hollow fibers, J. Membr. Sci. 77 (1993) 123–131.
[56] S. Stade, M. Kallioinen, A. Mikkola, T. Tuuva, M. Mänttäri, Reversible and irreversible compaction of ultrafiltration membranes, Separ. Purif. Technol. 118 (2013) 127–134.
[57] V.E. Reinsch, A.R. Greenberg, S.S. Kelley, R. Peterson, L.J. Bond, A new technique for the simultaneous, real-time measurement of membrane compaction and performance during exposure to high-pressure gas, J. Membr. Sci. 171 (2000) 217–228.
[58] I.H. Huisman, B. Dutré, K.M. Persson, G. Trägårdh, Water permeability in ultrafiltration and microfiltration: viscous and electroviscous effects, Desalination 113 (1997) 95–103.
[59] M. Aghajani, S.H. Maruf, M. Wang, J. Yoshimura, G. Pichorim, A. Greenberg, Y. Ding, Relationship between permeation and deformation for porous membranes, J. Membr. Sci. 526 (2017) 293–300.
[60] M.C. Saha, H. Mahfuz, U.K. Chakravarty, M. Uddin, M.E. Kabir, S. Jeelani, Effect of density, microstructure, and strain rate on compression behavior of polymeric foams, Mater. Sci. Eng., A 406 (2005) 328–336.
[61] L.J. Gibson, M.F. Ashby, Cellular Solids: Structure and Properties, Cambridge University Press, 1999.
[62] S.J. Tao, Positronium annihilation in molecular substances, J. Chem. Phys. 56 (1972) 5499–5510.
[63] M. Eldrup, D. Lightbody, J.N. Sherwood, The temperature dependence of positron lifetimes in solid pivalic acid, Chem. Phys. 63 (1981) 51–58.
[64] T. Fujioka, N. Oshima, R. Suzuki, W.E. Price, L.D. Nghiem, Probing the internal structure of reverse osmosis membranes by positron annihilation spectroscopy: gaining more insight into the transport of water and small solutes, J. Membr. Sci. 486 (2015) 106–118.
[65] F.A. Pacheco, I. Pinnau, M. Reinhard, J.O. Leckie, Characterization of isolated polyamide thin films of RO and NF membranes using novel TEM techniques, J. Membr. Sci. 358 (2010) 51–59.
[66] T.E. Culp, Y.-x. Shen, M. Geitner, M. Paul, A. Roy, M.J. Behr, S. Rosenberg, J. Gu, M. Kumar, E.D. Gomez, Electron tomography reveals details of the internal microstructure of desalination membranes, Proc. Natl. Acad. Sci. Unit. States Am. 115 (2018) 8694.
[67] L. Lin, R. Lopez, G.Z. Ramon, O. Coronell, Investigating the void structure of the polyamide active layers of thin-film composite membranes, J. Membr. Sci. 497 (2016) 365–376.
[68] S. Karan, Z. Jiang, A.G. Livingston, Sub–10 nm polyamide nanofilms with ultrafast solvent transport for molecular separation, Science 348 (2015) 1347–1351.
[69] D.R. Paul, The role of membrane pressure in reverse osmosis, J. Appl. Polym. Sci. 16 (1972) 771–782.
[70] D.R. Paul, Reformulation of the solution-diffusion theory of reverse osmosis, J. Membr. Sci. 241 (2004) 371–386.
[71] K.A.-S. Jönsson, B.T.L. Jönsson, Fluid flow in compressible porous media: I: steady-state conditions, AIChE J. 38 (1992) 1340–1348.
[72] R. Everaers, K. Kremer, Elastic properties of polymer networks, Mol. Model. Ann. 2 (1996) 293–299.
[73] M. Rubinstein, S. Panyukov, Nonaffine deformation and elasticity of polymer networks, Macromolecules 30 (1997) 8036–8044.
[74] T. Edvinsson, C. Elvingson, G.A. Arteca, Variations in molecular compactness and chain entanglement during the compression of grafted polymers, Macromol. Theory Simul. 9 (2000) 398–406.
[75] L. Gong, S. Kyriakides, Compressive response of open cell foams Part II: initiation and evolution of crushing, Int. J. Solid Struct. 42 (2005) 1381–1399.
[76] M.N. Sarbolouki, I.F. Miller, On pore flow models for reverse osmosis desalination, Desalination 12 (1973) 343–359.
[77] A. Mehta, A.L. Zydney, Permeability and selectivity analysis for ultrafiltration membranes, J. Membr. Sci. 249 (2005) 245–249.
[78] D.M. Kanani, W.H. Fissell, S. Roy, A. Dubnisheva, A. Fleischman, A.L. Zydney, Permeability–selectivity analysis for ultrafiltration: effect of pore geometry, J. Membr. Sci. 349 (2010) 405–410.
[79] H.K. Lonsdale, R.L. Riley, C.R. Lyons, D.P. Carosella, Transport in composite reverse osmosis membranes, in: M. Bier (Ed.), Membrane Processes in Industry and Biomedicine: Proceedings of a Symposium Held at the 160th National Meeting of the American Chemical Society, under the Sponsorship of the Division of Industrial and Engineering Chemistry, Chicago, Illinois, September 16 and 17, 1970, Springer US, Boston, MA, 1971, pp. 101–122.
[80] G.Z. Ramon, M.C.Y. Wong, E.M.V. Hoek, Transport through composite membrane, part 1: is there an optimal support membrane? J. Membr. Sci. 415–416 (2012) 298–305.
[81] J. Wang, D.S. Dlamini, A.K. Mishra, M.T.M. Pendergast, M.C.Y. Wong, B.B. Mamba, V. Freger, A.R.D. Verliefde, E.M.V. Hoek, A critical review of transport through osmotic membranes, J. Membr. Sci. 454 (2014) 516–537.
[82] K. Wang, A.A. Abdalla, M.A. Khaleel, N. Hilal, M.K. Khraisheh, Mechanical properties of water desalination and wastewater treatment membranes, Desalination 401 (2017) 190–205.
[83] Q. She, J. Wei, N. Ma, V. Sim, A.G. Fane, R. Wang, C.Y. Tang, Fabrication and characterization of fabric-reinforced pressure retarded osmosis membranes for osmotic power harvesting, J. Membr. Sci. 504 (2016) 75–88.
[84] X. Li, S. Zhang, F. Fu, T.-S. Chung, Deformation and reinforcement of thin-film composite (TFC) polyamide-imide (PAI) membranes for osmotic power generation, J. Membr. Sci. 434 (2013) 204–217.
[85] L. Gong, S. Kyriakides, W.Y. Jang, Compressive response of open-cell foams. Part I: morphology and elastic properties, Int. J. Solid Struct. 42 (2005) 1355–1379.
[86] T.G. Nieh, K. Higashi, J. Wadsworth, Effect of cell morphology on the compressive properties of open-cell aluminum foams, Mater. Sci. Eng., A 283 (2000) 105–110.
[87] L. Xia, J. Ren, M. Weyd, J.R. McCutcheon, Ceramic-supported thin film composite membrane for organic solvent nanofiltration, J. Membr. Sci. 563 (2018) 857–863.
[88] P.S. Singh, S.V. Joshi, J.J. Trivedi, C.V. Devmurari, A.P. Rao, P.K. Ghosh, Probing the structural variations of thin film composite RO membranes obtained by coating polyamide over polysulfone membranes of different pore dimensions, J. Membr. Sci. 278 (2006) 19–25.